Pergamon

Acta Materialia 50 (2002) 3743–3755

Acta MATERIALIA

www.actamat-journals.com

Mechanical deformation of dendrites by fluid flow during the solidification of undercooled melts

Kalin Dragnevski, Andrew M. Mullis *, Daniel J. Walker, Robert F. Cochrane

Department of Materials, University of Leeds, Leeds LS2 9JT, UK

Received 21 February 2002; received in revised form 29 April 2002; accepted 14 May 2002

Abstract

Mechanical interactions between growing dendrites and their parent melt are normally considered to be of little significance. During conventional solidification processing this is undoubtedly true. However, during the solidification of undercooled melts the twin conditions required to produce mechanical damage to dendrites, high flow velocities and very fine dendrites, may exist. This is most likely in strongly partitioning alloy systems where the tip radius experiences a local minimum at undercoolings in the range of 50–100 K. In this paper we present a model for the skin stress resulting from fluid flow around a family of realistically shaped dendrites. We find that within a narrow undercooling range about the minimum in the tip radius, mechanical deformation of the growing dendrite is likely. Experimental evidence is presented from the Cu–3wt%Sn and Cu–O alloy systems that appear to show evidence of extensively deformed dendritic structures consistent with mechanical damage. Other mechanisms for causing dendritic bending during growth are considered and shown to be unlikely in this case. © 2002 Acta Materialia Inc. Published by Elsevier Science Ltd. All rights reserved.

Keywords: Rapid solidification; Alloys: copper; Microstructure; Theory and modelling

1. Introduction

It is widely accepted within the metallurgical community that fluid flow during solidification can have no mechanical effect on growing dendrites, although thermo-solutal effects may be significant. Indeed, Pilling & Hellawell [1], writing in 1996, stated that ‘there are no reports of which we are aware of dendritic arms being mechanically bent’. During conventional solidification processing the evidence, both experimental and theoretical, in support of this view is compelling. However, during the solidification of undercooled melts the combined conditions of very fine dendrites and high flow velocities for mechanically damaged dendrites may be satisfied.

As a pure metal solidifies from its undercooled parent melt the radius of curvature at the dendrite tip, R, will decrease monotonically with increasing undercooling, ΔT. However, in alloy systems, particularly those in which one component is strongly partitioning, the situation is more complex. In this case, R will experience a local minimum, typically at undercoolings in the range of

* Corresponding author. Fax: +44-113-242-2531.
E-mail address: a.m.mullis@leeds.ac.uk (A.M. Mullis).

1359-6454/02/$22.00 © 2002 Acta Materialia Inc. Published by Elsevier Science Ltd. All rights reserved.
PII: S1359-6454(02)00186-6

50–100 K. This local minimum is indicative of the transition from solutally controlled at low growth velocity to coupled thermo-solutal growth at intermediate growth velocity. Typical growth velocities for this transition are of the order 1 m $s^{-1} \leq V \leq 3$ m s^{-1}. It is in the vicinity of this local minimum in R that the greatest likelihood of observing mechanically damaged dendrites exists.

Many of the techniques for processing undercooled melts also provide the high fluid velocities that are required if mechanical damage is to occur. During the growth phase significant shrinkage induced flow will occur. Shrinkage voids are rare in samples processed at low undercooling and consequently it would seem reasonable to assume that shrinkage flow is such that continuity is maintained at the solid–liquid interface. For a dendrite growing at velocity V the maximum shrinkage flow velocity V_s is given by

$$V_s = V\delta \quad (1)$$

where δ is the volume change upon melting. Taking a typical value [2] of $\delta \approx 0.05$ for an FCC metal with $V \approx 2$ m s^{-1} we have $V_s = 0.01$ m s^{-1}.

Heating of metallic melts by electromagnetic induction is known to produce potentially vigorous stirring of the melt. The likely magnitude of this stirring has been studied in detail for processing by electromagnetic levitation, where flow rates of the order of 0.3 m s^{-1} are expected [3–5], but is much less well characterised when induction heating is utilised in other containerless processing techniques. In the work reported here we use a fluxing technique to produce undercooled melts. Heating of the melt is by means of an induction heated graphite susceptor, with a 2 mm wall thickness. At the working frequency of the induction heater used (450 kHz) a solid susceptor of this wall thickness would transmit around 50% of the electromagnetic power directly to the sample. However, as the susceptor actually used in the experiments had two viewing slots cut in line-of-sight with the sample, the actual power transmitted during experiments probably exceeded this level. Consequently, taking 0.3 m s^{-1} as typical of the flow velocity expected during electromagnetic levitation (in which the sample experiences no electromagnetic screening) we believe that an estimate of the flow velocity in our samples of the order 0.1 m s^{-1} may not be unreasonable during experiments with $\approx$50% screening.

A number of other effects common in the processing of undercooled melts may, however, tend to mask the observation of deformed dendritic structures. In particular, many alloys will tend to undergo a spontaneous transition from a coarse columnar structure to a fine grained equiaxed structure and then back to a columnar structure as the undercooling is progressively increased. Unfortunately this region of equiaxed grain structure coincides with the local minimum in R, making the observation of any potential deformation impossible in these systems. This transition is unlikely however to be related to any mechanical deformation taking place during the growth phase [6,7]. However, by use of an appropriate model of spontaneous grain refinement [8], suitable alloy systems that do not grain refine can be identified.

In a recent paper, Battersby et al. [9] presented the results of a comparative study of the solidification of undercooled Cu, Cu–O and Cu–Sn melts. In one of these samples, a Cu–3wt%Sn alloy undercooled by 73 K, there was evidence of a deformed dendritic structure which, we believe, may have resulted from mechanical damage to the growing dendrites. In this paper we present further evidence from the study of the Cu–3wt%Sn system, together with a new system, Cu–O, which seems to provide compelling evidence of bent dendritic structures. We then present a detailed mechanical model which shows that mechanical bending of dendrites is possible. Finally, we consider the possibility that an alternative mechanism, thermosolutal advection, could have given rise to the observed bending and find this to be unlikely.

2. Experimental procedure

Melt fluxing was chosen as the most suitable means to study the alloy systems under consideration, as the melting point of Cu-based alloys is generally too low for significant undercoolings to be achieved by electromagnetic levitation. The method allows high undercoolings to be achieved as nucleation on the container walls is prevented

by isolating the melt from these surfaces. The flux can also aid the removal of oxide impurities from the melt by dissolution in the flux and protects the surface from oxidation.

Undercooling experiments were performed within a stainless steel vacuum chamber evacuated to a pressure of 10^{-6} mbar and backfilled to 500 mbar with N_2 gas. Samples were heated, in silica crucibles, by induction heating of a graphite susceptor contained within an alumina radiation shield. Viewing slots were cut in the susceptor and alumina to allow the sample to be viewed during the experiment. A commercial soda-lime glass was employed as the flux to reduce the number of potential sites for heterogeneous nucleation. The temperature was monitored by means of a k-type thermocouple positioned at the base of the crucible, which had been thinned, thus reducing the thermal lag between the sample and the thermocouple. Heating and cooling curves were obtained by using a chart recorder. A schematic diagram of the fluxing apparatus is shown in Fig. 1. By using this method it was possible to achieve temperatures of up to 1473 K, thus easily accommodating melting and superheating of the alloy systems that were to be investigated, ensuring that the samples were completely contained within the glass flux.

Copper samples of 99.9999% purity (metal basis) were obtained from ALFA (Johnson Matthey). However, these samples contain a residual level of oxygen. Based on the work of previous researchers, we have defined Cu–O alloys as Cu containing at least 200 ppm of oxygen after undercooling and oxygen free copper as containing less than 200 ppm of oxygen.

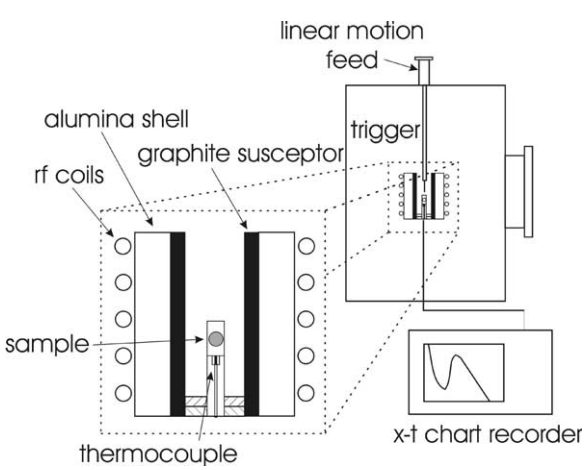

Fig. 1. Schematic diagram of the fluxing apparatus.

A Cu–3wt%Sn alloy was prepared by arc melting under argon. All starting materials were obtained from ALFA (Johnson Matthey) and were of 99.9999% purity. In order to ensure complete mixing of the elements and to eliminate any segregation the alloy was re-melted and finally annealed at 1023 K for 30 min.

After undercooling, the as-solidified droplets were mounted in Bakelite, then polished and finally etched in an appropriate solution to reveal structure and substructure. Optical microscopy was carried out on a Nikon Optiphot microscope using bright field (BF), differential interference contrast (DIC) mode and polarized light. Scanning electron microscopy was performed on a CamScan Series 4 SEM. Vickers microhardness measurements were carried out on the polished specimens using a Photoplan microhardness tester, applying a load of 100 gf for 30 s.

3. Experimental results

The first system chosen for study was Cu–O. Fig. 2a reveals the microstructure of a sample undercooled by 47 K. The dendritic substructure is highly irregular and consists of a large number of bent primary and secondary dendrite arms. Another interesting feature within the microstructure of the sample can be seen at the bottom left hand corner of the micrograph. The grain that separates the dendrites via a faceted grain boundary is thought to be an inter-penetrant grain. It has been suggested that the formation of such grains during non-equilibrium solidification is caused by the growth of dendrites in different directions [10]. If dendrite arms are bent by randomly directed flows during growth, the formation of such grains is not unlikely. Fig. 2b shows the microstructure of the same sample under polarized light: a more contrasting topography of the dendritic structure is displayed. At higher magnifications (Fig. 2c, DIC mode) an array of deformed secondary arms can be seen, together with the inter-penetrant grain, which

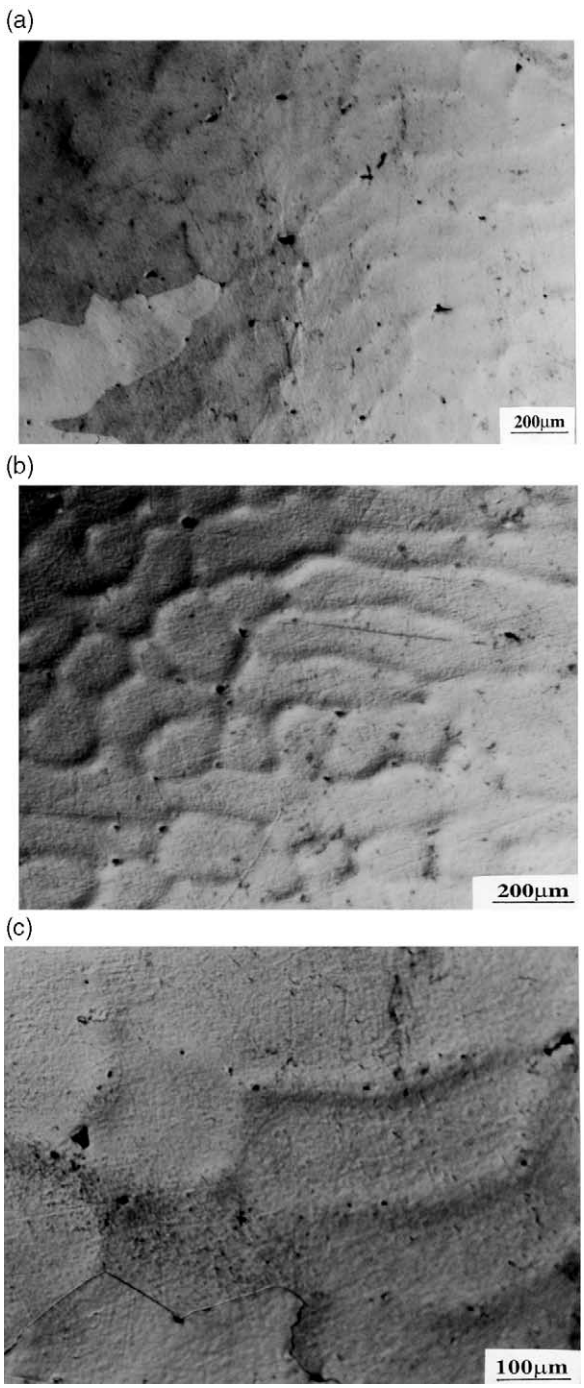

Fig. 2. Optical micrographs of a Cu–O sample undercooled by 47 K prior to nucleation: (a) bright field image; (b) under polarized light; (c) under DIC mode (etched in acidified potassium dichromate).

provides strong evidence that the dendritic structure has been mechanically damaged.

The same microstructural effect was observed in the Cu–3wt%Sn alloy system, previously studied by Battersby et al. [9]. It was suggested that the microstructures observed within this undercooling range consisted of a not fully developed dendritic network. Fig. 3 depicts the microstructure of a Cu–3wt%Sn sample undercooled by 70 K prior to nucleation. The combination of appropriate etchant (acidified potassium dichromate) and differential interference contrast reveals that the dendritic structure is, in fact, well developed and appears to be deformed, although the deformation is not as well defined as that observed in the Cu–O alloy system. It is also apparent that at this level of undercooling, it is difficult to identify the primary dendrite trunks, although it is clear that the secondary dendrite arms are bent and fragmented.

At higher undercoolings the dendritic substructure revealed, proved again to be highly deformed. Fig. 4 shows the microstructure of the Cu–3wt%Sn sample undercooled by 85 K prior to nucleation. Within the microstructure, no grain boundaries are observed associated with substructure, i.e. this is not a fine array of subgrains. Moreover, at this undercooling, the dendritic network is fully developed and the primary and secondary dendrite arms can clearly be defined. It can be seen that the secondary arms have been deformed during growth

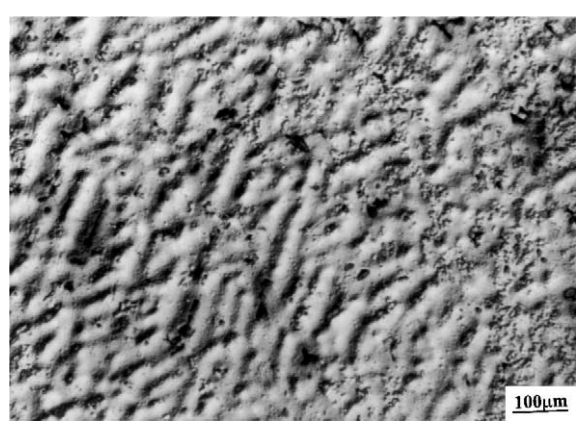

Fig. 3. Optical micrograph of a Cu–3wt%Sn sample undercooled by 70 K prior to nucleation (DIC mode, etched in acidified potassium dichromate).

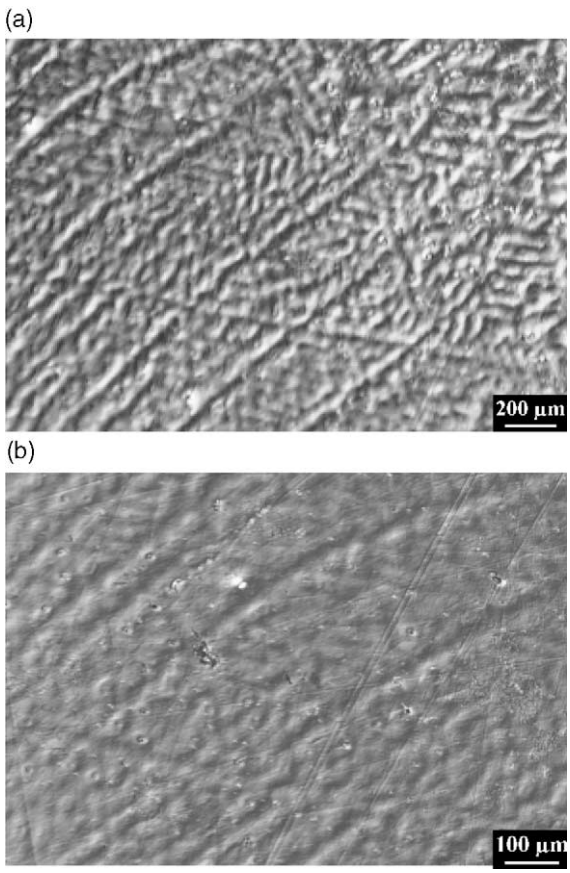

Fig. 4. Optical micrographs of the Cu–3wt%Sn sample undercooled by 85 K prior to nucleation: (a) DIC-mode; (b) under polarized light at higher magnifications (etched in acidified potassium dichromate).

from the undercooled melt, most probably due to fluid flow effects.

As the undercooling is increased, growth of deformation-free dendrites takes place, yielding a structure of well-developed columnar dendrites, as shown in Fig. 5 for the Cu–3wt%Sn alloy system. At undercoolings above 100 K, a columnar dendritic structure is revealed with no evidence of bent dendrites. The primary and secondary dendrite arms can clearly be seen and the microsegregtion pattern is very well defined (Fig. 6).

The structure of the Cu–3wt%Sn alloy remains essentially unchanged up to ΔT=183 K. Above this undercooling Battersby et al. showed that grain refinement by recrystallisation takes place. The

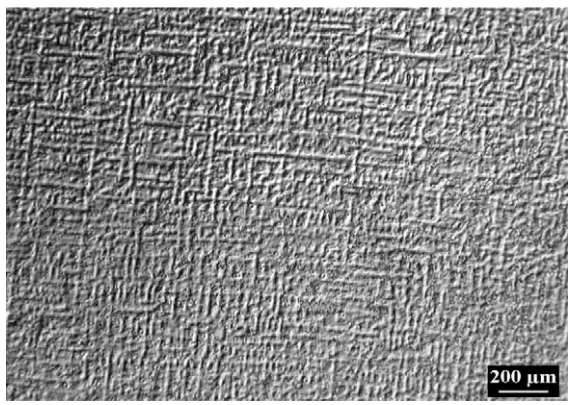

Fig. 5. Optical micrograph of a Cu–3wt%Sn sample undercooled by 91 K prior to nucleation (DIC-mode, etched in acidified potassium dichromate).

same applies for the Cu–O alloy system, where grain refined microstructures were observed at undercoolings above 90 K[9].

Previous studies [11] on the Cu–Sn system (with up to 6 wt% Sn) showed that at very low undercoolings, solidification proceeded via the growth of columnar dendrites that exhibited a very well defined microsegregation pattern. It was suggested that this was due to the large interval between the solidus and liquidus lines and the low diffusion coefficient of Sn in Cu. For the Cu–O system it was shown that at undercoolings below 40 K the grain size was very coarse and the substructure consisted of well developed dendrites with coarse secondary arm spacing and no evidence of bending and the presence of inter-penetrant grains.

To further understand the microstructure–undercooling relationship, microhardness measurements were made on the Cu–3wt%Sn samples solidified at various undercoolings. Results from these measurements are shown in Fig. 7. The microhardness increases to a maximum value of 148 kgf/mm^2 at an undercooling of 85 K, then decreases with further increases in undercooling, to 106 kgf/mm^2 at an undercooling of 104 K and then increases again with further increases in undercooling up to a value of 133 kgf/mm^2. The increase in microhardness at low undercoolings strongly suggests that the microstructure has been deformed, which is consistent with the optical microscopy

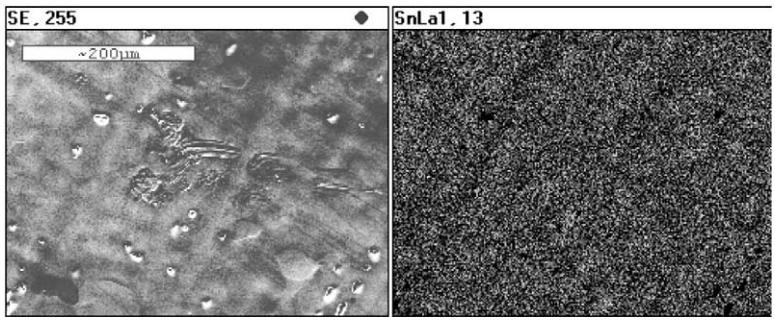

Fig. 6. SEM micrograph and X-ray maps of the Cu–3wt%Sn sample undercooled by 104 K prior to nucleation.

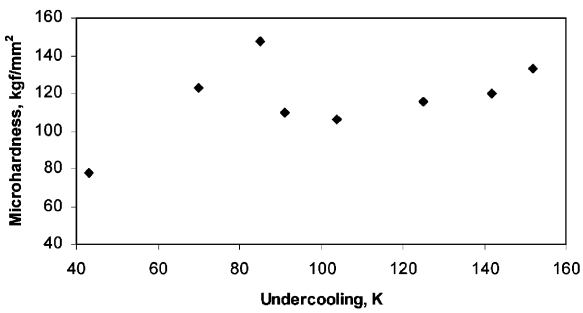

Fig. 7. Microhardness as a function of undercooling for the Cu–3wt%Sn alloy.

observations. The following decrease in microhardness is due to the fact that at the undercoolings, solidification progresses via the growth of deformation-free dendrites, which again is consistent with the optical microscopy analysis. At undercoolings above 100 K the microhardness increases again due to a decrease in substructure size and an increase of point and/or line defects.

In summary, it can be said that microscopical examination of undercooled samples from the Cu–O and Cu–Sn alloy systems suggests that within a narrow undercooling range, between 45 and 85 K, deformation of dendrites is apparent. In the Cu–O system, this deformation appears to be centred around an undercooling of 50 K, while in Cu–3wt%Sn the maximum deformation occurs at a somewhat higher undercooling, around 85 K. Microhardness measurements in Cu–3wt%Sn are consistent with increasing levels of stress in the as-solidified samples as the undercooling is increased, with a local maximum close to 85 K.

4. A model of flow induced stress in dendritic structures

An analytical model of the flow induced stress within a dendrite, modelled as a semi-infinite cylinder of revolution of diameter *d*, has been given by Pilling and Hellawell [1]. In this paper we use a somewhat more realistic geometrical model for the dendrite geometry. Solutions to the flow equations are obtained numerically, using a commercial computational fluid dynamics (CFD) code, CFX 4.1 [12]. The results thus obtained are compared with those of Pilling and Hellawell.

4.1. Dendrite geometry

In considering the dendritic structure that would result from the solidification of an alloy system it is clear that one of the regions most likely to show deformation is the secondary arms. This is because the secondary arms often show highly constricted growth where they attach to the primary trunk. This is a result of growing through the enriched solute layer that surrounds the primary trunk. Consequently, the base of a secondary dendrite arm is much narrower, and hence may be deformed more easily, than either the middle of the secondary arm or the primary trunk. An assessment of whether dendrite deformation is possible has thus been made on the basis of flow around a secondary arm with a constriction at its base. In this respect we are following the earlier work of Pilling and Hellawell.

In defining a geometrical model of a secondary arm belonging to an alloy dendrite we have

imposed the following constraints. The dendrite, which we take to be a figure of revolution of unit height, should have a smooth, continuously differentiable surface with a radius minimum r_1, at z_1, and a radius maximum r_2, at z_2. Moreover, we require $dr/dz \rightarrow 0$ as $z \rightarrow 0$ and $dr/dz = 0$ at $z = 1$. The following parametric function can be shown to satisfy all of these criteria

$$\bar{\mathbf{Z}}(t,\theta) = \begin{pmatrix} x(t)\cos(\theta) \\ x(t)\sin(\theta) \\ z(t) \end{pmatrix} 0 \leq \theta \leq 2\pi \tag{2}$$

where

$$x = a_0(a_1 t + a_2 t^2 + a_3 t^3 + a_4 t^4)\ t \geq 0 \tag{3}$$

$$z = \exp(-t^2)\ t \geq 0 \tag{4}$$

and

$$a0 = (\alpha^2\beta^2(3\alpha\beta(\alpha-\beta) + \beta^3 - \alpha^3))^{-1} \tag{5}$$

$$a_1 = 2\alpha\beta(\beta^4 r_1 - \alpha^4 r_2) + 4\alpha^2\beta^2(\alpha^2 r_2 - \beta^2 r_1) \tag{6}$$

$$a_2 = \alpha^5 r_2 - \beta^5 r_1 + \alpha\beta(\alpha^3 r_2 - \beta^3 r_1 + 8\alpha\beta(\beta r_1 - \alpha r_2)) \tag{7}$$

$$a_3 = 2(\beta^4 r_1 - \alpha^4 r_2) + 4\alpha\beta(\alpha^2 r_2 - \beta^2 r_1 + \alpha\beta(r_2 - r_1)) \tag{8}$$

$$\alpha_4 = \alpha^3 r_2 - \beta^3 r_1 + 3\alpha\beta(\beta r_1 - \alpha r_2) \tag{9}$$

$$\alpha = \sqrt{-\ln(z_1)} \tag{10}$$

$$\beta = \sqrt{-\ln(z_2)} \tag{11}$$

Fig. 8 shows a representative example of the geometry produced by this parametric representation. With an appropriate choice of the parameters r_1, r_2, z_1 and z_2, geometries which are in good agreement with both observed secondary arm goemetries in transparent analogue systems [13] and phase-field simulations of alloy solidification [14] can be generated.

4.2. Equations of flow

If we assume that the liquid metal acts as an incompressible Newtonian fluid with viscosity μ

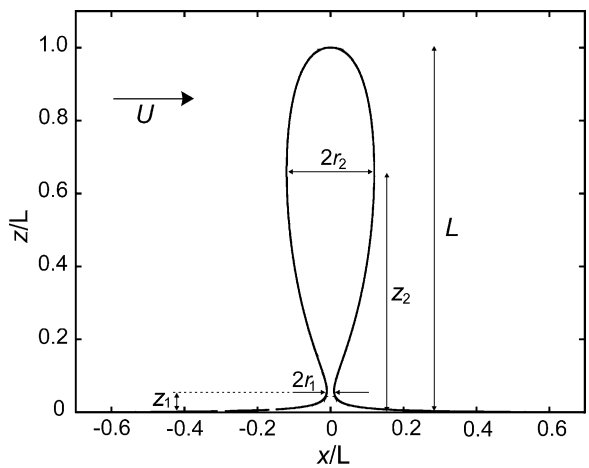

Fig. 8. The geometrical model used to represent a dendrite in the flow calculation.

and velocity $\bar{u} = (u,v,w)$, the steady-state equations of flow are given by

$$\nabla \cdot \bar{u} = 0 \tag{12}$$

and

$$\rho(\bar{u}\cdot\nabla)\bar{u} = \nabla \cdot \bar{\bar{\sigma}} \tag{13}$$

where ρ is the density of the fluid.

The stress tensor for an incompressible Newtonian fluid is given by

$$\bar{\bar{\sigma}} = -p\bar{\bar{I}} + \mu(\nabla\bar{u} + [\nabla\bar{u}]^{\mathrm{T}}) \tag{14}$$

where $\bar{\bar{I}}$ is the unit tensor and p is the fluid pressure.

Solutions to the flow equations, subject to the boundary conditions described below, are obtained numerically with the commercial CFD code CFX 4.1, utilising the control volume cell method in which Cartesian co-ordinates, x^i, in physical space undergo a non-singular mapping to non-orthogonal co-ordinates ξ^i in computational space using a generalisation of the Rhie and Chow formulation.

In Cartesian co-ordinates Eq. (13) is

$$\frac{\partial}{\partial x^i}(\rho u^i u^k) = \frac{\partial}{\partial x^i}\sigma^{ik} \tag{15}$$

where σ^{ik} is the stress tensor

$$\sigma^{ik} = -p\delta^i_k + \mu\left(\frac{\partial u^i}{\partial x^k} + \frac{\partial u^k}{\partial x^i}\right). \tag{16}$$

This implies that

$$\frac{\partial}{\partial x^i}\left(\rho u^i u^k - \mu\frac{\partial u^k}{\partial x^i}\right) = -\frac{\partial \rho}{\partial x^k} + \frac{\partial}{\partial x^i}\left(\mu\frac{\partial u^i}{\partial x^k}\right) \tag{17}$$

$$\frac{\partial}{\partial x^i} J^i_{u^k} = S_{u^k} \tag{18}$$

where the total flux vectors and source terms are given by

$$J^i_{u^k} = \rho u^i u^k - \mu\frac{\partial u^k}{\partial x^i} \tag{19}$$

and

$$S_{u^k} = -\frac{\partial \rho}{\partial x^k} + \frac{\partial}{\partial x^i}\left(\mu\frac{\partial u^i}{\partial x^k}\right) \tag{20}$$

Eq. (20) is the general form of the scalar advection-diffusion equation. Keeping the velocity components, u^i, in the fixed Cartesian directions the transformation into computational space proceeds as

$$\frac{\partial}{\partial \xi^i}\hat{J}^i_{u^k} = \sqrt{g}S_{u^k} \tag{21}$$

with

$$\hat{J}^i_{u^k} = \rho\hat{u}^i u^k - \Gamma^{ij}\frac{\partial u^k}{\partial \xi^i} \tag{22}$$

$$\Gamma^{ij} = \mu\sqrt{g}g^{ij} \tag{23}$$

where g^{ij} is the metric tensor for the control volume cell and $\sqrt{g}$ is the volume of the corresponding cell. Full details of the computational scheme are given in Ref. [15]

4.3. Flow boundary conditions

For a dendrite of unit height, as described by Eq. (2), the computational domain extends from $-6\leq x\leq 6$, $-6\leq y\leq 6$ and $0\leq z\leq 6$. The maximum diameter of the dendrite used in any of the simulations was 0.3. Boundary conditions are specified within the computational domain as follows. On the upstream boundary (y–z plane at $x=-6$) we apply a constant flux condition, which is equivalent to fluid entry at constant velocity U aligned along the x-direction (i.e. orthogonal to the principal axis of the dendrite)

$$\bar{u}(x=-6,y,z) = \begin{pmatrix} U \\ 0 \\ 0 \end{pmatrix} \tag{24}$$

while on the downstream boundary (y–z plane at $x=6$) fluid exit is via a zero pressure boundary

$$p(x=6,y,z) = 0. \tag{25}$$

No slip conditions are applied at all solid surfaces, that is

$$\bar{u}(\bar{\mathbf{Z}}) = 0 \tag{26}$$

where $\bar{\mathbf{Z}}$ is the locus defined by Eq. (2). All other domain walls are zero flux boundaries.

4.4. Calculation of the bending moment

Values for the shear stress acting along the tangent to the surface of the dendrite due to drag, $\tau_{r\theta}$ and hydrostatic pressure, $P_{r\theta}$, are obtained from the stress tensor $\bar{\bar{\sigma}}$ for the converged solution. Following Pilling and Hellawell we may write the force acting in the x-direction, F_x, as

$$Fx(z,\theta) = \tau_{r\theta}(z)\sin(\theta) + \mathrm{P}_{r\theta}(z)\cos(\theta) \tag{27}$$

wherein the total force, $F(z)$, acting on the dendrite at height z is given by

$$F(z) = \int_0^{2\pi} F(z,\theta)r(z)\mathrm{d}\theta \tag{28}$$

The skin stress in the dendrite arm, as a function of position, is given by

$$\sigma(z) = \frac{M(z)r(z)}{I[r(z)]} \tag{29}$$

where $M(z)$ is the bending moment and $I(z)$ the moment of inertia of the section at z. Assuming the dendrite bends about its narrowest point, r_1, these are

$$M(z_1) = \int_{z_1}^{1} -F(z)(z-z_1)\mathrm{d}z \tag{30}$$

and

$$I[r(z_1)] = \frac{\pi[r(z_1)^4]}{4}. \quad (31)$$

4.5. Dendrite radius as a function of undercooling

No well-defined route exists for calculating the radius of a secondary dendrite arm as a function the undercooling at which it grew. However, where dendritic growth has been observed directly, in transparent analogue casting systems such as succinonitrile [16] and xenon [17], the evidence is that the morphology of dendrites grown at different undercoolings is probably self-similar when scaled against the tip radius, R. Consequently, many of the more obvious length scales of the dendrite are simple multiples of R, and this technique has previously been used by a number of authors to estimate the dimensions of various dendritic features [8,18]. Here we assume our secondary dendrite arms are a fixed multiple of R, which we estimate from marginal stability theory.

If we assume that the thermal conductivities in the solid and liquid, κ_l and κ_s, are equal we may write

$$R = \frac{\Gamma}{\sigma^* \Delta T_{hyp} Pt F(A_c)} \quad (32)$$

where A_c and $F(A_c)$ are two dimensionless quantities first suggested by Lipton et al. [19]

$$A_c = \frac{1}{1-(1-k)Iv(Pc)} \quad (33)$$

$$F(A_c) = \xi_l + \frac{2\xi_c D_t m C_o c_p A_c (1-k)}{H D_l} \quad (34)$$

with

$$\Gamma = \frac{\gamma T_l}{\rho H} \quad (35)$$

where γ is the interfacial energy between the solid and liquid phases, T_l the liquidus temperature, D_l is the thermal diffusivity in the liquid phase, m the slope of the liquidus line, C_o the alloy concentration and k the partition coefficient. Pt is the thermal Peclet number in the liquid

$$Pt = \frac{VR}{2D_l}. \quad (36)$$

The equivalent solutal Peclet number is given by

$$Pc = \frac{VR}{2D_c} \quad (37)$$

where D_c is the solutal diffusivity in the liquid.

Due to solute trapping at the interface at high growth rates, k will be related to the equilibrium partition coefficient, k_e, by [20]

$$k(V) = \frac{k_e + aV/D_l}{1 + aV/D_l} \quad (38)$$

where a is the Aziz solute trapping parameter and k_e is defined such that $m(1-k_e) < 0$. $\sigma*$ is a stability constant which, for a plane interface, Mullins and Sekerka [21] give as $1/4\pi^2$. The dimensionless quantities ξ_l and ξ_c are given by

$$\xi_l = 1 - \frac{1}{\sqrt{1 + \frac{1}{\sigma^* Pt^2}}} \quad (39)$$

and

$$\xi_c = 1 + \frac{2k_e}{1-2k_e - \sqrt{1 + \frac{1}{\sigma^* Pc^2}}}. \quad (40)$$

Iv is the Ivantsov function [22]

$$Iv(Pt) = Pt \exp(Pt) Ei(-Pt) \quad (41)$$

where Ei is the exponential integral function.

4.6. Estimation of the yield stress for Cu–3at%Sn at its melting point

The flow shear stress, as a function of the homologous temperature, T/T_l, has been obtained from the deformation maps of Frost and Ashby [23]. At the low undercoolings at which dendritic deformation was observed, the plateau time, that is the time between recalescence and complete solidification of the sample, was of the order of a few seconds. For bending sufficient to be evident in the as-solidified sample (say $\geq 30°$) to have occurred

within the available time the shear strain rate would have been of the order $10^{-1}-10^{-2}$ s^{-1}. At these strain rates the required shear stress for pure copper at its melting temperature is estimated as $(2.3–3.5)\times10^{-4}$ $\mu_s(T_l)$, where $\mu_s(T_l)$ is the shear modulus at the liquidus temperature.

Over most of the homologous temperature range μ_s decreases linearly with T. Certainly this appears to be a very good approximation up to $T/T_l=0.6$. As far as we are aware the shear modulus of copper has not been measured close to its melting point. If the linear trend from low temperature data were continued, we estimate, from the data of Frost and Ashby that $\mu_s(T_l)\approx24$ GPa. However, in many materials the elastic moduli decrease rapidly as the melting temperature is approached and this value may thus be considerably in excess of the true value. Using this value we deduce that an upper bound on the flow stress for pure copper at its melting point may be of the order of 7 MPa. In the absence of experimental data we have assumed that the value for the dilute Cu–O and Cu–Sn alloys will be of the same order.

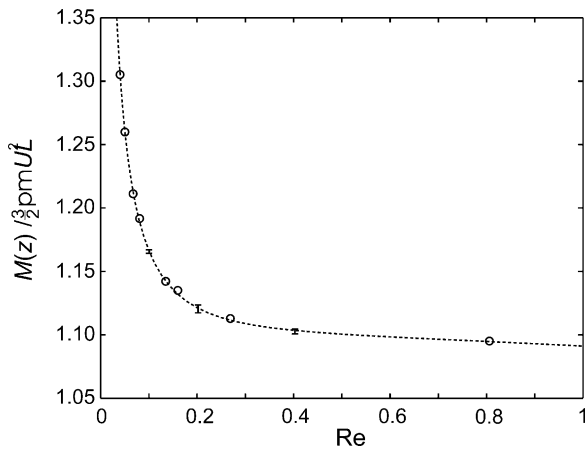

Fig. 9. Comparison of the results of the numerical flow model with the analytical model of Pilling and Hellawell as a function of the Reynolds number for the flow. Good agreement between the two is apparent, particularly at high Reynolds number. The numerical model exceeds the analytical model due to the fact that the analytical model considers flow around a semi-infinite body and thus ignores drag around the end of the dendrite.

5. Results

5.1. Comparison of the numerical model with the analytical model of Pilling and Hellawell

For a semi-infinite cylinder Pilling and Hellawell found the force per unit length due to the flow of a fluid with velocity U orthogonal to the principal axis of the dendrite to be

$$F = 3\pi\mu U \tag{42}$$

which is independent of the radius of the cylinder. This gives a bending moment for a cylinder of length L of

$$M = \frac{FL^2}{2} = \frac{3}{2}\pi\mu UL^2 \tag{43}$$

In Fig. 9 we present the results of our numerical calculation of M as a function of the Reynolds number, Re, for the flow

$$Re = \frac{V_f\rho l}{\mu} \tag{44}$$

where l is a characteristic length scale for the problem. Pilling and Hellawell chose the diameter of the cylinder as their characteristic length scale so for the purposes of direct comparison with the analytical model we have chosen to take the diameter of the dendrite at its widest point, $2r_2$, as the characteristic length scale.

It is apparent from the figure that agreement between the relatively simple analytical model of Pilling and Hellawell and the numerical model presented here is generally very good, particularly at higher Reynolds numbers, where the models agree to within 10%. We suspect that the small discrepancy that does exist between the models arises largely due to the fact that we are considering flow around a body of finite length, which includes drag effects around the end of the dendrite. The location and size of the maximum and minimum radius were found to have virtually no effect on the calculated value of M. Parameters were varied within the limits $0.02\leq r_1\leq 0.055$ and $0.05\leq z_1\leq 0.09$, the effect of this variation being indicated by the error bars in Fig. 9.

5.2. Flow stress as a function of undercooling in Cu melts

To estimate the skin stress in a dendrite growing from an undercooled melt we have adopted the following procedure. The tip radius as a function of undercooling is estimated from Eq. (32), and this is used to set the length scale for the problem, with r_1, r_2 and L all being fixed multiples of R. Schwarz et al.[8] found that the ratio of calculated tip radius to measured dendrite trunk radius was approximately 20 with a standard deviation of 10, this result being independent of undercooling. Here we have assumed $r^2 = 20R$. Analysis of images of ripened dendrites grown from transparent analogue casting systems indicates that $r_1 = r_2/4$ and $L = 10r_2$ would not be unreasonable [13]. While we have not undertaken a full sensitivity analysis of how σ will vary with these parameters, we consider that they are generally conservative and will serve to give an indication of the likely stress levels present. Most of the other parameters in the model can be obtained in a fairly straightforward manner. m and k_e can be obtained from the equilibrium phase diagrams for Cu–O and Cu–Sn and have been taken here as $C_o = 0.08$ at.%, $m = 46.2$ K at.%$^{-1}$ and $k_e = 0.013$ for Cu–O and $C_o = 3.0$ wt%, $m = 6.1$ K wt%$^{-1}$ and $k_e = 0.145$ for Cu–Sn. All other material parameters have been assumed to be typical of elemental Cu and are readily available in the literature [2], with the exception of γ and a, which we have taken as $\gamma = 0.223$ J m^{-2} and $a = 2 \times 10^{-10}$ m. The general validity of the parameter set has been checked by comparing the predicted growth velocities with the measured recalescence velocities reported by Battersby et al. [9] for the same systems.

The bending moment on the dendrite is estimated from

$$M = \frac{3}{2}\psi(Re)\pi\mu UL^2 \tag{45}$$

where $\psi(Re)$ is the ratio of the numerical and analytical bending moments calculated above which can be read off from Fig. 9. Utilising this procedure, an estimate of the skin stress in the dendrite at its neck is given in Fig. 10a and b as a function of undercooling and flow velocity in the melt for Cu–Sn and Cu–O. For completeness, the calculated dendrite tip radius is also shown (dashed curve, right hand axis) as is the estimated yield stress of 7 MPa. It is apparent from the figures that in both cases the skin stress peaks very sharply close to the region in which we observed deformed dendrites in the as-solidified sample, around 75 K for Cu–3wt%Sn and close to 50 K for Cu–O. This is clearly the result of the decrease in tip radius associated with the onset of solute trapping. In Cu–3wt% Sn a flow velocity of 0.1 m s^{-1} causes the

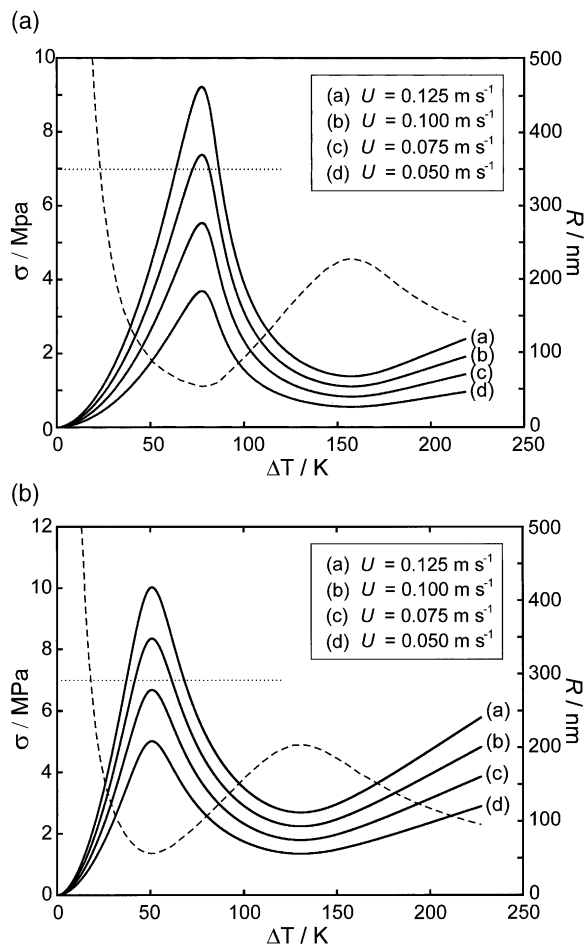

Fig. 10. The estimated skin stress in the dendrite as a function of undercooling and flow velocity for (a) the Cu–3wt%Sn alloy and (b) the Cu–O alloy. Also indicated is the calculated dendrite tip radius, R (dashed curve, right-hand axis) and the likely upper bound of 7 MPa on the yield stress for flow at shear rates of the order 10^{-1}–10^{-2} s^{-1} (dotted line).

peak skin stress to exceed our estimated upper bound of the stress required to cause deformation in a narrow window centered around $\Delta T = 77$ K. For higher flow velocities, or conversely a lower value of the yield stress, this window in which deformation may occur is enlarged. In Cu–O, the peak skin stress corresponding to a flow velocity of 0.1 m s^{-1} is much higher, 12 MPa. This is consistent with the experimental results in that the deformation observed in the Cu–O samples appears much more severe and extensive than in the Cu–3wt%Sn samples. We also note the very close correspondence in the shape of the skin stress and microhardness curves for Cu–3wt%Sn (Figs. 10a and 7, respectively) which would suggest the microhardness is a direct record of the stress the sample was subject to during solidification.

6. Alternative bending mechanisms

Finally, we should consider the possibility that the deformed structures observed arise as the result of some other mechanism. The most likely such mechanism is thermo-solutal advection, in which perturbation of the isotherms (or isoconcentrate lines) by the flow field results in bending of the growing dendrite arms. The effects of flow on dendritic growth by thermo-solutal advection have been studied by Mullis [24], for the case in which the principal growth and flow directions are aligned orthogonally. This analysis revealed that thermal/solutal advection did indeed cause a rotation of the principal growth direction into the flow. Moreover, for small deflections of the tip, the deflection, Δx, is proportional to Δt^2. This is consistent with the angle of the outward normal to the tip, θ, being rotated at a constant rate. As the growth velocity is also constant, Δx is proportional to Δz^2, that is θ is proportional to Δz. This is most conveniently expressed as

$$\Delta x = \Phi(\Delta z)^2 \tag{46}$$

where Φ gives the rotation of the principal growth direction per unit length of growth. Mullis found that Φ is a function of two variables, $\Phi = \Phi(Pt_f, Pt_g)$, where Pt_g and Pt_f are the are the Peclet numbers for growth and flow, with Pt_g as defined by Eq. (36) and Pt_f given by

$$Pt_f = \frac{UR}{2D_l} \tag{47}$$

Φ was found to vary linearly with Pt_f and as $(Pt_g)^b$, with $b \approx -1.85$. Using the measured growth velocities reported by Battersby et al. [9[9]] and the calculated values of the tip radii we estimate the growth and flow Peclet numbers for Cu–O at 50 K to be of the order of 5×10^{-3} and 4×10^{-4}, respectively. The equivalent values for Cu–3wt% Sn at 73 K are of the same order. Extrapolating from the data of Mullis [24] we obtain a value for Φ of 7.5×10^{-3} rad m^{-1}. As the features reported are typically 500 μm or less, this corresponds to a maximum deflection of the principal growth direction of 2×10^{-4} degrees. Consequently we conclude that the effect of flow induced bending due to thermo-solutal advection during solidification is negligible and that consequently any deformation observed is likely to be mechanical.

7. Summary and conclusions

Under most conditions encountered within solidification processing the likelihood of dendrites experiencing mechanical damage due to flow of the parent melt is remote. However, during the processing of undercooled melts the conditions of both very fine dendrites and potentially high flow velocities required to initiate such damage may exist. Using the example systems, Cu–O and Cu–3wt%Sn, we have shown that conditions could exist wherein mechanical damage may occur. Damage is likely to be confined within a narrow undercooling range, centered on the undercooling where the dendrite tip radius passes through a local minimum. This is around 50 K in Cu–O and somewhat higher at 75–85 K in Cu–3wt%Sn. Microstructural evidence is presented from both of these systems which appear to show deformed dendritic structures. The deformation is confined to the predicted low undercooling window and is generally rather more extensive in the Cu–O system than in Cu–3wt%Sn, again in line with model predictions. In Cu–3wt%Sn microhardness measurements have

been made on samples solidified at different levels of undercooling. These show an increase in microhardness with undercooling up to a local maximum around 85 K, wherein the microhardness falls abruptly before increasing again slowly with undercooling. The general shape of this curve is remarkably similar to the calculated stress curve for Cu–3wt%Sn and is suggestive that microhardness acts as a direct record of the solidification stress induced in the sample.

References

[1] Pilling J, Hellawell A. Metall Mater Trans 1996;27A:229–32.
[2] Iida T, Guthrie RIL. The physical properties of liquid metals. Oxford: Clarendon, 1988.
[3] El-Kaddah N, Szekely J. Metall. Trans. 1983;14B:401–10.
[4] El-Kaddah N, Szekely J. Metall. Trans. 1984;15B:183–6.
[5] Schwartz E, Szekely J, Ilegbusi O, Zong JH, Egry I. In: Szekely J, editor. Magnetohydrodynamics in process metallurgy. Warrendale, PA: Metallurgical Society of AIME; 1992. p. 81–7.
[6] Mullis AM, Cochrane RF. J Appl Phys 1997;82:3783–90.
[7] Mullis AM, Cochrane RF. J Appl Phys 1998;84:4905–10.
[8] Schwarz M, Karma K, Eckler K, Herlach DM. Phys Rev Lett 1994;73:1380–3.
[9] Battersby SE, Cochrane RF, Mullis AM. J Mater Sci 2000;35:1365–73.
[10] Battersby SE. PhD thesis, University of Leeds; 1997.
[11] Rashkov N. In: Metallography and heat treatment of metals. Sofia: Technika; 1988. p. 7-2.
[12] Computational Fluid Dynamics Services, AEA Technology, Harwell, UK.
[13] Hellawell AI. In: Kirkwood DH, Kapranos P, editors. Proceedings of the 4th International Conference on Semi-Solid Processing of Alloys and Composites; Sheffield, UK. 1996. p. 60–5.
[14] Warren JA, Boettinger WJ. Acta metall. mater. 1995;43:689–703.
[15] CFX 4.1 Flow solver guide. Harwell, UK: AEA Technology; 1995.
[16] Corrigan DP, Koss MB, La Combe JC, DeJager KD, Tennenhouse LA, Glicksman ME. Phys. Rev. E 1999;60:7217–23.
[17] Bisang U, Bilgram JH. Phys. Rev. E 1996;54:5309–26.
[18] Pan QY, Huang WD, Lin X, Zhou YH. J. Cryst. Growth 1997;181:109–16.
[19] Lipton J, Kurz W, Trivedi R. Acta metall. 1987;35:957–64.
[20] Aziz MJ. J Appl Phys 1982;53:1158–68.
[21] Mullins WW, Sekerka RF. J Appl Phys 1964;33:444–51.
[22] Ivantsov GP. Doklady Akademii Nauk SSSR 1947;58:567–9.
[23] Frost HJ, Ashby MF. In: Deformation-mechanism maps. Oxford, UK: Pergamon; 1982. p. 24–5.
[24] Mullis AM. Acta mater 1999;47:1783.